Nanoscale Advances

ROYAL SOCIETY OF CHEMISTRY

PAPER

View Article Online
View Journal | View Issue

Cite this: *Nanoscale Adv.*, 2021, **3**, 5618

Turbulence enhanced ferroelectric-nanocrystal-based photocatalysis in urchin-like $TiO_2/BaTiO_3$ microspheres for hydrogen evolution†

Haidong Li, *[a] Yanyan Song,[a] Jiyun Zhang[a] and Jiating He[b]

Received 6th May 2021
Accepted 15th July 2021

DOI: 10.1039/d1na00331c

rsc.li/nanoscale-advances

The application of a built-in electric field due to piezoelectric potential is one of the most efficient approaches for photo-induced charge transport and separation. However, the efficiency of converting mechanical energy to chemical energy is still very low, and the enhancement of photocatalysis, thus, is limited. To overcome this problem, here, we propose sonophotocatalysis based on a new hybrid photocatalyst, which combines ferroelectric nanocrystals ($BaTiO_3$) and dendritic TiO_2 to form an urchin-like $TiO_2/BaTiO_3$ hybrid photocatalyst. Under periodic ultrasonic excitation, a spontaneous polarization potential of $BaTiO_3$ nanocrystals in response to ultrasonic waves can act as an alternating built-in electric field to separate photoinduced carriers incessantly, which can significantly enhance the photocatalytic activity and cyclic performance of the urchin-like $TiO_2/BaTiO_3$ catalyst. More importantly, the significant enhancement of photocatalytic hydrogen evolution is due to the coupling effect of two types of piezoelectric potential in the presence of $BaTiO_3$ nanocubes as well as the semiconductor and optical properties of TiO_2 nanowires of the urchin-like $TiO_2/BaTiO_3$ hybrid structure under simulated sunlight and periodic ultrasonic irradiation, which can significantly improve the efficiency of converting mechanical energy to chemical energy.

1. Introduction

TiO_2 is one of the highly efficient photocatalytic hydrogen production catalysts. It has been widely studied as one of the most important photocatalysts since 1972.[1–11] However, TiO_2 only absorbs ultraviolet (UV) light in a broad solar spectrum due to its large bandgap energy ($\lambda < 380$ nm), which comprises only ~3% of sunlight.[12–14] Many efforts have focused on the development of broadband response nanomaterials with spectrum response from the UV to the visible,[10,15–24] and even to the infrared (IR) region.[18,20,25–29] Apart from the improvement in light absorption, increasing the photo-carrier transport and separation ability is also one of the most important ways to improve photocatalytic performance.[30–33] One of the main measures to achieving these objectives is the construction of semiconductor heterostructures based on Schottky junctions, P–N junctions and band structure alignment, which can build the internal electric field at the interface of the heterostructure due to their different energy band properties that are required to achieve charge transport and separation.[32,34–39] For example: 1. Commercial P25 (composite structure of rutile and anatase);[13,40] 2. TiO_2 core–shell structure energy band;[5,40] 3. TiO_2 heterostructures.[3,13,41–44] In addition, by preparing TiO_2 polyhedrons with different exposed crystal facets, carrier transfer is generated by using different crystal face level structures.[12,45–47] The former method has certain limitations in promoting carrier separation. The latter method is mainly to synthesize TiO_2 polyhedral single crystals. Although some strategies based on heterostructures have been designed and put into practice to solve these types of problem, the photocatalytic efficiency is still too low to transfer and separate electron–hole pairs completely during photocatalysis. The enhancement of the photocatalysis is limited to block its practical application. In order to further improve the photocatalytic efficiency and expand the light response, renewing the built-in electric field and maintaining the photoinduced carrier transport and separation incessantly during the photocatalysis process is the greatest challenge for maintaining high performance of the photocatalyst with an internal field.

Based on the theory of piezophotonics and sonophotochemical synthesis and their application in the field of photocatalysis,[48–57] the spontaneous polarization of the piezoelectric $BaTiO_3$ materials forms a surface potential along the polarization.[55] And our previous research has reported that by introducing Ag_2O nanoparticles to the surface of the $BaTiO_3$ piezoelectric material, the photo-induced charge in the photocatalyst can be effectively separated.[58] Stimulation *via* external ultrasound results in surface free-charge saturation of $BaTiO_3$ nanocubes. Thus, it shows an obvious charge separation to

[a]*College of Materials Science and Engineering, Qingdao University, Qingdao, 266071, PR China. E-mail: haidongli@qdu.edu.cn*

[b]*Institute of Materials Research and Engineering, A*STAR, Singapore 138634*

† Electronic supplementary information (ESI) available. See DOI: 10.1039/d1na00331c

eliminate the self-reduction of Ag_2O with improved photocatalytic degradation performance.

In this paper, we report the development of ferroelectric-enhanced photocatalysis on the basis of an urchin-like TiO_2/$BaTiO_3$ hybrid catalyst under periodic ultrasonic excitation. Through a simple hydrothermal method, nanosized TiO_2 nanowires with a length of 200–300 nm and width of 5–10 nm were uniformly and epitaxially assembled to the surface of tetragonal $BaTiO_3$ nanocubes forming an urchin-like TiO_2/$BaTiO_3$ hybrid structure. The spontaneous electrical polarization on the $BaTiO_3$ nanocube increased the band bending of TiO_2 nanowires and enhanced the charge generation and separation efficiency. In the meantime, the piezoelectric effect combined with spontaneous electrical polarization and photoelectric conversion realizes an ultrasonic wave driven piezophototronic process in the urchin-like TiO_2/$BaTiO_3$ hybrid photocatalyst, which is the fundamental to sono-photocatalysis resulting in improved redox reactions. This research provided a successful demonstration of the ferroelectric effect in nanostructured heterojunctions as an effective strategy for improving the photocatalysis in H_2 generation.

2. Experimental

2.1 Chemicals

The chemical reagents used for the synthesis of $BaTiO_3$, urchin-like TiO_2 nanostructures and urchin-like TiO_2/$BaTiO_3$ hybrid nanostructures were commercially available. Titanium isopropoxide (TTIP, 98%), ethylene glycol (EG, 99%), and cetyltrimethyl ammonium bromide (CTAB, 99%) were purchased from Sigma-Aldrich Co. LLC. Hydrochloric acid (HCl, 36%), $Ba(OH)_2 \cdot 8H_2O$ (98%), NaOH (98%) and KOH (98%) were purchased from China National Medicines Corporation Ltd, as well as commercialized Degussa P25 (TiO_2, *ca.* 20% rutile and 80% anatase). All chemicals were used without further purification.

2.2 Preparation of tetragonal and cubic $BaTiO_3$ nanocubes

Tetragonal $BaTiO_3$ nanocubes were synthesized through a composite-hydroxide-mediated approach.[59] A mixture of 20 g anhydrous hydroxides (NaOH/KOH = 51.5 : 48.5) was put into a 25 mL Teflon-lined autoclave, followed by the addition of 0.6 mmol $BaCl_2$ and 0.5 mmol TiO_2. The autoclave was then sealed and heated at 200 °C for 48 h. After reaction, the autoclave was taken out to cool to room temperature. The intermediate product was dissolved, filtered and then washed thoroughly with deionized water and dilute hydrochloric acid (0.05 M) to remove excessive hydroxide and barium carbonate.

Cubic $BaTiO_3$ nanocubes were synthesized through a hydrothermal method. The mixture of TiO_2 (3.99 g, 0.05 mol), $Ba(OH)_2 \cdot 8H_2O$ (94.5 g, 0.3 mol) and 3 mL deionized water was transferred to a Teflon-lined autoclave. The autoclave was heated to 200 °C and kept for 5 days. After hydrothermal treatment, the autoclave was cooled to room temperature. The intermediate product was dissolved, filtered and washed thoroughly with deionized water and dilute hydrochloric acid (0.05 M).

2.3 Synthesis of the urchin-like TiO_2 and urchin-like TiO_2/$BaTiO_3$ hybrid catalyst

Urchin-like TiO_2 nanostructures were prepared by a simple hydrothermal method. In a typical experimental procedure, 0.28 g TTIP was added into 13.8 g concentrated HCl solution with vigorous stirring (A), and 0.22 g CTAB was added into 27.3 mL distilled water to form CTAB aqueous solution (B). After stirring for 30 min, solution B was added into A and the mixture was stirred for 1 h to form the TTIP aqueous solution. Then, 0.3 g (5 mmol) urea was added into the autoclave. The total volume of the aqueous TTIP solution and EG (TTIP/EG = 1 : 3 in volume) was kept at 20 mL. The hydrothermal reaction was carried out at 150 °C for 20 h. The product was purified by washing and centrifugation with ethanol, and then dried at 80 °C for 24 h.

Urchin-like TiO_2/$BaTiO_3$ hybrid nanostructures were prepared by the same procedures described above. In a typical experimental procedure, 0.28 g TTIP was added into 13.8 g concentrated HCl solution with vigorous stirring (A), and 0.22 g CTAB was added into 27.3 mL distilled water to form aqueous CTAB solution (B), then 100 mg of $BaTiO_3$ nanocubes was dispersed in B. After ultrasonic treatment for 30 min, solution B was added into A and stirred for 1 h to form the TTIP aqueous solution. Then, 0.3 g (5 mmol) urea was added into the autoclave. The total volume of the aqueous TTIP solution and EG (TTIP/EG = 1 : 3 in volume) was kept at 20 mL. The hydrothermal reaction was carried out at 150 °C for 20 h. The product was purified by washing and centrifugation with ethanol and then dried at 80 °C for 24 h.

2.4 Characterization

X-ray powder diffraction (XRD) patterns of the samples were recorded on a Bruker D8 Advance powder X-ray diffractometer with Cu Kα (λ = 0.15406 nm). A Hitachi S-4800 field emission scanning electron microscope (FE-SEM) was used to characterize the morphology of the samples. High resolution transmission electron microscopy (HRTEM) and scanning transmission electron microscopy (STEM) images were acquired with a JOEL JEM 2100F. X-ray photoelectron spectroscopy (XPS) was performed using an Escalab 250.

2.5 Catalytic activity of the urchin-like TiO_2/$BaTiO_3$ hybrid catalyst

The sonocatalytic, photocatalytic and sonophotocatalytic activity of urchin-like TiO_2/$BaTiO_3$ hybrid nanostructures was investigated by H_2 evolution experiments under ultrasound and/or light irradiation in a gas closed circulation system. In a typical reaction, 100 mg of the catalyst powder was dispersed in CH_3OH aqueous solution using a magnetic stirrer (80 mL of distilled water and 20 mL of CH_3OH). A commercial solar simulator (300 W) equipped with a Xe lamp was used as the light source for photocatalytic H_2 generation. The power density of the incident light was about 100 $mW \cdot cm^{-2}$ and the experiment was also equipped with a stepless frequency ultrasonic generator (50 W). Hydrogen gas was measured using an on-line

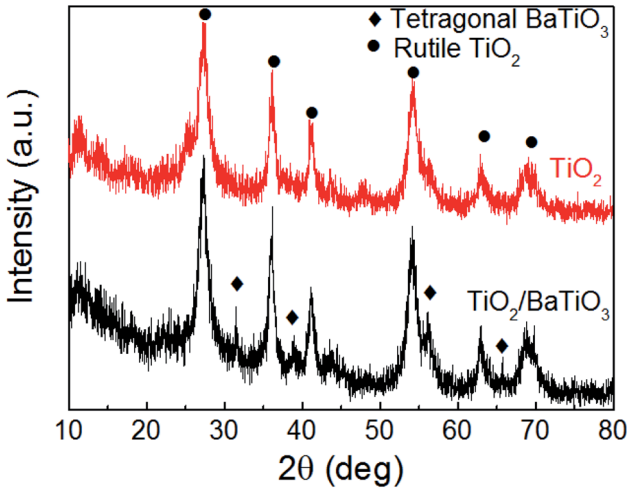

Fig. 1 XRD patterns of the as-synthesized products: urchin-like TiO_2 and urchin-like $TiO_2/BaTiO_3$ hybrid catalyst.

gas chromatograph (GC-7900, Argon as a carrier gas) equipped with a thermal conductivity detector (TCD).

3. Results and discussion

X-ray diffraction (XRD) characterization was conducted to characterize the crystallography of urchin-like TiO_2 and urchin-like $TiO_2/BaTiO_3$ hybrid catalyst. The red curve in Fig. 1 revealed that the crystal phase of urchin-like TiO_2 is rutile with the diffraction peaks at about $2\theta = 27.5°$, $36.1°$, $41.2°$, $54.3°$ and $61.7°$, which could be perfectly indexed to the (110), (101), (111), (211), and (022) crystal faces of rutile TiO_2 (PDF card no. 21-1276). After the TiO_2 was assembled on tetragonal $BaTiO_3$ nanocubes by a simple hydrothermal method (black curve shown in Fig. 1), the additional tetragonal $BaTiO_3$ nanocube (PDF card no. 74-1963) diffraction peaks with 2θ values of $31.6°$, $38.9°$, $56.3°$, and $66.0°$ appeared, corresponding to (110), (111), (211), and (220) crystal planes, respectively, which indicates that a portion of rutile TiO_2 successfully covered the tetragonal $BaTiO_3$ nanocubes. Interestingly, the XRD peaks attributed to TiO_2 in the $BaTiO_3/TiO_2$ composites do not shift compared with the pure TiO_2, from which it could be deduced that the Ba atoms do not substitute Ti and enter into the TiO_2 lattices. Therefore, it is obvious that the synthesis route is favorable for obtaining a multicomponent oxide composite integrating rutile phase TiO_2 with the tetragonal phase $BaTiO_3$. Moreover, from the black curve, we found that the peak intensity of $BaTiO_3$ is weak, indicating that a part of the $BaTiO_3$ surface may be covered by TiO_2. The inference was also validated by the XPS analysis. The fully scanned spectra and enlarged signals of Ba 3d, Ti 2p and O 1s of the urchin-like $TiO_2/BaTiO_3$ hybrid catalyst are illustrated in Fig. 2. The peaks related to the Ba and Ti core level and Auger peaks, the O 1s and Auger peaks, and small carbon peaks due to contaminants that contain C can be spotted. The high resolution XPS spectrum of the Ba 3d peak

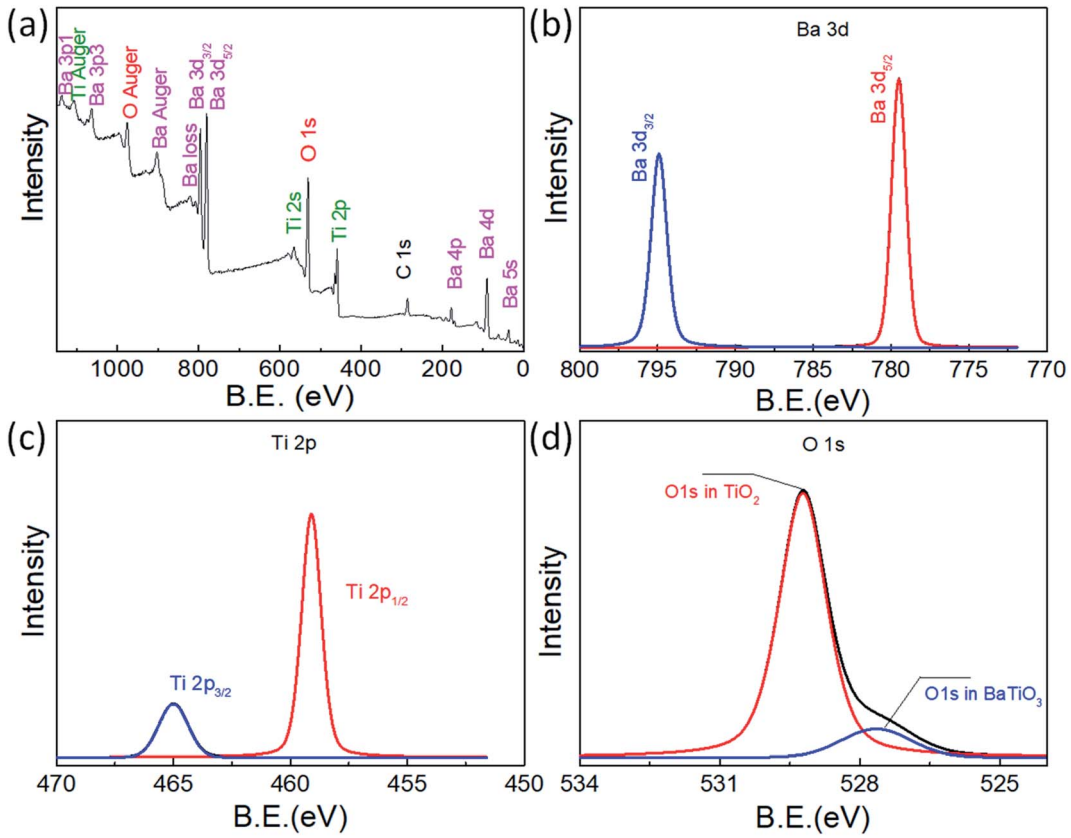

Fig. 2 XPS spectra of the urchin-like $TiO_2/BaTiO_3$ hybrid catalyst. (a) Survey spectra of the urchin-like $TiO_2/BaTiO_3$ hybrid catalyst, and enlarged signals of (b) Ba 3d, (c) Ti 2p and (d) O 1s.

can be resolved into two components (Ba $3d_{3/2}$ at 794.6 eV and Ba $3d_{5/2}$ at 779.0 eV), which correspond to the barium in $BaTiO_3$. The Ti 2p peak can be resolved into two components (Ti $2p_{3/2}$ and Ti $2p_{1/2}$), which are located at around 458.3 eV and 464.2 eV, corresponding to the titanium in $BaTiO_3$ and TiO_2. The O 1s response splits into two peaks at around 529.2 eV and 526.7 eV, which is consistent with oxygen in the form of O 1s in TiO_2 and O 1s in $BaTiO_3$, respectively. The XPS results demonstrate that the hybrid materials are also composed of $BaTiO_3$ and TiO_2.

The morphology and structure of the urchin-like TiO_2 and urchin-like $TiO_2/BaTiO_3$ hybrid catalyst were investigated by scanning electron microscopy (SEM). Fig. 3a and b present the morphology and structure of the as-grown nanowires in urchin-like TiO_2 microspheres obtained through a simple hydrothermal method, and the diameter of the urchin-like TiO_2 microspheres is about 1 μm to 2.5 μm. After the TiO_2 nanowires assembled into $BaTiO_3$ nanocubes, the morphology of urchin-like $TiO_2/BaTiO_3$ hybrid microspheres was well preserved and could be observed from the SEM images (Fig. 3c and d). Fig. 3c shows that tetragonal $BaTiO_3$ nanocubes are covered by the TiO_2 nanowires, and the resulting 3D structure of $TiO_2/BaTiO_3$ hybrid microspheres with a diameter of about 1 μm was synthesized and has better monodispersity and a smaller diameter compared with urchin-like TiO_2 microspheres. This may be attributed to the $BaTiO_3$ nanocubes as a template for the growth of TiO_2 nanowires on it. The morphology of tetragonal $BaTiO_3$ nanocubes is discussed in detail (ESI S1 and S2†) in our previous paper.[58]

Transmission electron microscopy (TEM) images further confirm the formation of urchin-like $TiO_2/BaTiO_3$ hybrid microspheres. In Fig. 4, the nanosized TiO_2 nanowires (sea urchin-like tentacles) 200–300 nm in length and 5–10 nm in width are grown on the surface of tetragonal $BaTiO_3$ nanocubes uniformly, forming urchin-like $TiO_2/BaTiO_3$ hybrid microspheres.

Fig. 4 shows the TEM images of urchin-like $TiO_2/BaTiO_3$ hybrid microspheres. Both the SEM (Fig. 3) and TEM images indicate that the diameters of the TiO_2 nanowires are around 5–10 nm with a narrow size distribution. The crystal structure and the growth direction of TiO_2 nanowires were then examined by HRTEM analysis together with the corresponding fast Fourier transform (FFT) patterns (Fig. 4c). As evidenced by the HRTEM images, the nanowires are single crystals, and the observed lattice fringes demonstrate that the growth of the nanowires was parallel to the (110) planes but perpendicular to the (001) planes and the corresponding interplanar distances are *ca.* 0.33 nm and 0.25 nm, respectively. Moreover, it is noteworthy that the morphology of the TiO_2 nanowires is not completely symmetrical on the tetragonal $BaTiO_3$ nanocube surface. This may be due to the electric field inside the tetragonal $BaTiO_3$ nanocube along its spontaneous polarization direction when the temperature goes below the Curie temperature ($T_c \sim 120$ °C)[60] during the synthesis cooling process. This spontaneous internal electric field may affect the crystal growth of the nanowires. These results suggest that the 3D hybrid microspheres are a well-crystallized heterostructure composed of TiO_2 nanowires and tetragonal $BaTiO_3$ nanocubes. As a comparison, the morphology and structure of cubic $BaTiO_3$ nanocubes are also discussed in detail (ESI S1 and S2†).

Fig. 5 presents the corresponding scanning transmission electron microscopy (STEM) images of urchin-like $TiO_2/BaTiO_3$ hybrid microspheres, and a line-profile analysis using STEM/

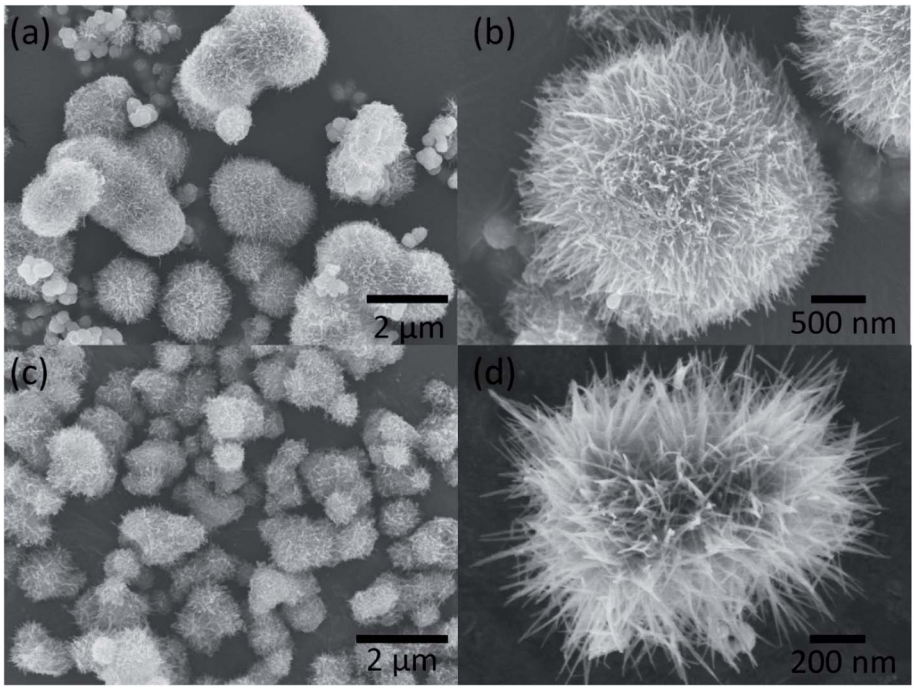

Fig. 3 SEM images of urchin-like TiO_2 microspheres (a and b) and urchin-like $TiO_2/BaTiO_3$ hybrid microspheres (c and d).

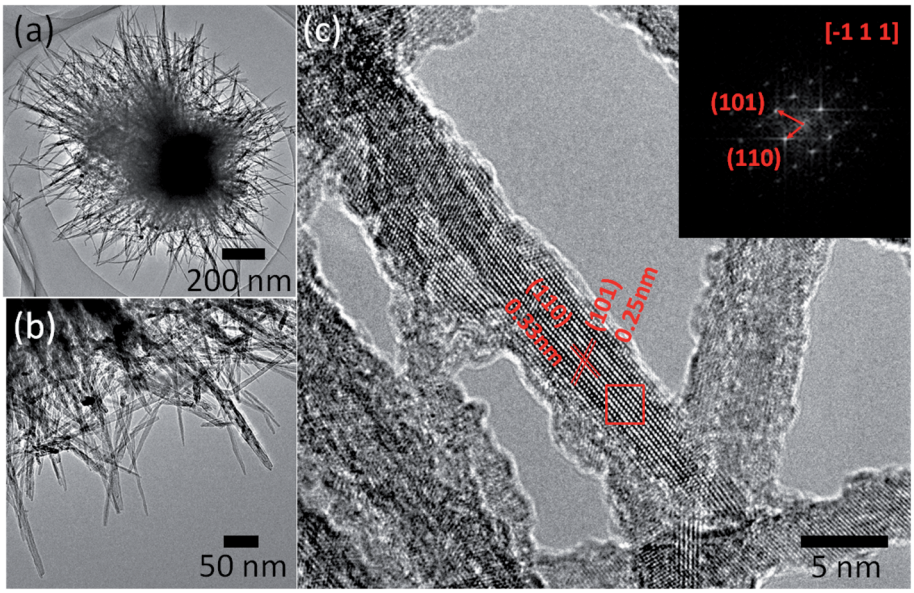

Fig. 4 (a and b) TEM images of urchin-like $TiO_2/BaTiO_3$ hybrid microspheres, (c) HRTEM image of a nanowire viewed along the [1–1–1] direction and fast Fourier transform pattern (inset). TEM images indicate that the diameters of the nanowires are distributed in a narrow range, around 5 nm.

energy-dispersive spectroscopy (EDS), revealing the distribution of the Ba, Ti and O components in the hybrid microspheres (Fig. 5a inset). The line profile analysis indicates that TiO_2 nanowires are distributed over the $BaTiO_3$ nanocubes, demonstrating the formation of an urchin-like $TiO_2/BaTiO_3$ hybrid microsphere structure. We obtained a similar EDS mapping graph (Fig. 5b) from urchin-like $TiO_2/BaTiO_3$ hybrid microspheres, EDS mapping images of urchin-like $TiO_2/BaTiO_3$ hybrid microspheres with individual elements of Ba, Ti and O, as well as the STEM image. These results further confirm that the TiO_2 nanowires are assembled on the surface of the tetragonal $BaTiO_3$ nanocubes.

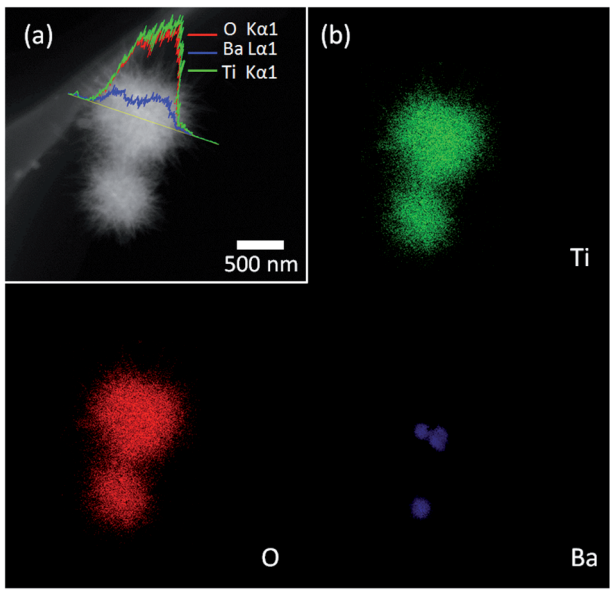

Fig. 5 STEM images (a) and EDS mapping (b) from urchin-like $TiO_2/BaTiO_3$ hybrid microspheres. Line profiles of elemental compositions measured by EDS along the line shown in the left side image (inset).

To evaluate the sonocatalytic, photocatalytic and sonophotocatalytic performance of the as-prepared samples, we evaluated the water splitting performance of pure tetragonal $BaTiO_3$, urchin-like TiO_2 microspheres and urchin-like $TiO_2/BaTiO_3$ hybrid microspheres under ultrasonic and/or simulated sunlight irradiation in methanol water solution. At first, for the sonocatalysis process, Fig. 6 shows the evolution of H_2 from the as-synthesized tetragonal $BaTiO_3$ nanocube and urchin-like $TiO_2/BaTiO_3$ hybrid microspheres, with an average rate of H_2 evolution of approximately 41.87 and 38.75 μmol g^{-1} h^{-1}, respectively, in the first vibration event (0–8 h). H_2 gas generation stops without ultrasonic irradiation (8–16 h, Fig S6 in ESI S3†) when the ultrasonic irradiation is off, $BaTiO_3$ nanocubes stop to generate hydrogen and oxygen without acoustic pressure and cavitation is induced by ultrasonic waves. After evacuating the reaction system and starting the ultrasonic irradiation again, a similar H_2 production rate is regained (16–24 h, Fig. S6 in ESI S3†). However, for urchin-like TiO_2 nanospheres without piezoelectric properties, the rate of sonocatalytic hydrogen production is almost zero under the ultrasonic radiation. As is well known, the water-splitting effect is thought to be powerful evidence of the release of free charge carriers into the reaction system. Combined with this, the results above indicate that the splitting reaction of the water can be induced by external mechanical energy without assistance of other forms of energy and demonstrate a strain-induced electric charge development on the tetragonal $BaTiO_3$ surface. Thus, an ultrasonic wave driven piezoelectric effect of ferroelectric $BaTiO_3$ nanocubes can induce the release of free charge carriers into the reaction system. It is consistent with the electro-catalysis mechanism of

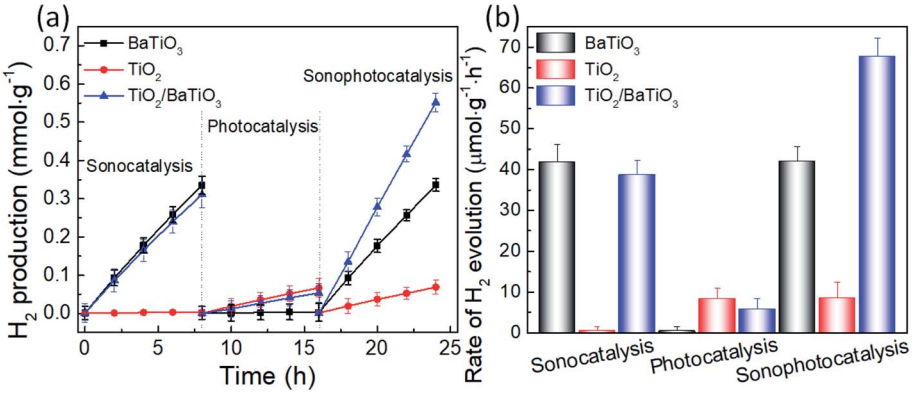

Fig. 6 (a) H_2 evolution performance as a function of irradiation time for sonocatalysis, photocatalysis and sonophotocatalysis in the presence of tetragonal $BaTiO_3$, urchin-like TiO_2 microspheres and urchin-like $TiO_2/BaTiO_3$ hybrid microspheres, and (b) the rate of H_2 evolution for the as-synthesized samples.

the piezoelectrochemical effect for the direct conversion of mechanical energy to chemical energy proposed by Kuang-Sheng Hong *et al.*[61,62] As a comparison, the hydrogen production performance of cubic $BaTiO_3$ without piezoelectric properties under ultrasonic irradiation is also discussed in detail (Fig. S6 in ESI S3†), further illustrating that tetragonal $BaTiO_3$ nanocubes have catalytic hydrogen production properties based on the piezoelectric effect under ultrasonic radiation. Moreover, in the sonocatalysis process, the hydrogen production rate of urchin-like $TiO_2/BaTiO_3$ hybrid microspheres is lower than that of tetragonal $BaTiO_3$ nanocubes under the ultrasonic radiation. This may be attributed to the lower content of $BaTiO_3$ with piezoelectricity in the urchin-like $TiO_2/BaTiO_3$ hybrid microspheres than that of tetragonal $BaTiO_3$ for a certain amount of total catalyst (100 mg). Apart from that above, to achieve good sonocatalytic or sonophotocatalytic (details below) performance for the urchin-like $TiO_2/BaTiO_3$ hybrid microspheres, the stability of this hybrid structure is crucial under ultrasonic treatment. ESI S3† illustrates that the TiO_2 nanowires are tightly attached on the surface of the $BaTiO_3$ nanocubes under ultrasonic treatment at 40 kHz, 50 W for 2 h in deionized water.

Secondly, for the photocatalysis process, to check the intrinsic photocatalytic properties of the samples, noble nanoparticles were not sputtered on the samples before hydrogen generation measurement. Fig. 6 shows the evolution of H_2 from the as-synthesized urchin-like TiO_2 microspheres and urchin-like $TiO_2/BaTiO_3$ hybrid microspheres, with an average rate of H_2 evolution of approximately 8.38 and 5.90 μmol g^{-1} h^{-1}, respectively, under simulated sunlight irradiation (8–16 h). In the meantime, the rate of H_2 evolution for tetragonal $BaTiO_3$ in the photocatalysis process is almost zero. The experimental results show that the urchin-like TiO_2 microspheres have higher photocatalytic hydrogen production activity than that of urchin-like $TiO_2/BaTiO_3$ hybrid microspheres. This may also be due to the different contents of TiO_2 under simulated sunlight irradiation, which is similar with that of the sonocatalysis process. Moreover, the H_2 evolution rates of the three catalysts are all relatively low under simulated sunlight irradiation (8–16 h, Fig. 6). This may be attributed to the large band gap of rutile TiO_2 (3.0 eV) and tetragonal $BaTiO_3$ (3.27 eV).

Finally, for the sonophotocatalysis process, the sonophotocatalytic activities of the as-prepared samples are also displayed (16–24 h, Fig. 6). Under irradiation of both ultrasonic and simulated light, the hydrogen generation rate of urchin-like $TiO_2/BaTiO_3$ hybrid microspheres is about 67.70 μmol h^{-1} g^{-1}, and Fig. S7 (ESI S3†) show the corresponding HPLC chromatograph of H_2 as a function of irradiation time in the presence of urchin-like $TiO_2/BaTiO_3$ hybrid microspheres with an effective mass of 100 mg in the system. Meanwhile, the hydrogen generation rate of the pure tetragonal $BaTiO_3$ and urchin-like TiO_2 microspheres is about 42.04 and 8.61 μmol h^{-1} g^{-1}, respectively. Together with the sonocatalysis and photocatalysis process discussed above, the urchin-like $TiO_2/BaTiO_3$ hybrid microspheres have the highest catalytic activity under three kinds of radiation conditions. Sonophotocatalysis experiment results proved that the spontaneous polarization potential of $BaTiO_3$ nanocubes can act as an alternating built-in electric field to transfer and separate photo-induced carriers produced by TiO_2 nanowires, which can successfully enhance the photocatalytic hydrogen evolution activity of the urchin-like $TiO_2/BaTiO_3$ hybrid photocatalyst. That demonstrates that the ultrasonic driven piezoelectric effect of ferroelectric $BaTiO_3$ nanocubes can significantly enhance photocatalysis in urchin-like $TiO_2/BaTiO_3$ hybrid microspheres by the release of free charge carriers into the reaction system. Furthermore, there is a three-way coupling effect of piezoelectric, semiconductor and photonic properties in urchin-like $TiO_2/BaTiO_3$ hybrid microspheres, using the piezoelectric potential that is generated by applying a strain to the $TiO_2/BaTiO_3$ hybrid semiconductor heterostructure with piezoelectricity, enhancing the carrier generation, transport, and separation. Moreover, the piezoelectric potential is generated not only from the direct ultrasonic radiation of the $BaTiO_3$ nanocubes, but also from the local turbulence generated by the ultrasonic action, which in turn generates a local water pressure that causes the TiO_2 nanowires to bend and further act on the bond between the TiO_2 nanowires and the $BaTiO_3$ nanocubes (Fig. S9†). Thus, the

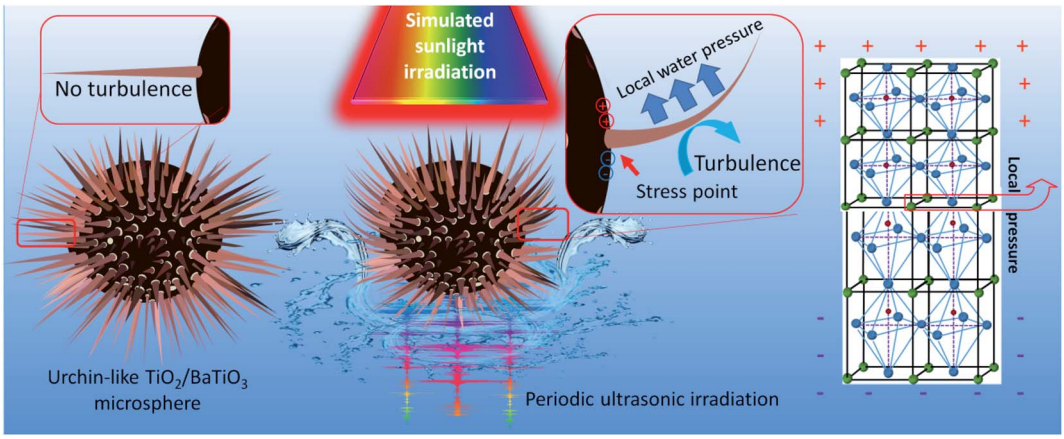

Fig. 7 Schematic diagram of sonophotocatalysis for the $TiO_2/BaTiO_3$ hybrid semiconductor heterostructure.

deformation of the $BaTiO_3$ nanocubes can be further increased and higher piezoelectric potential can be generated. At the same time, the $TiO_2/BaTiO_3$ composites synthesized with no addition of CTAB during the preparation process ($TiO_2/BaTiO_3(n)$) and Fig. S10† show its morphology (nearly spherical shape with no sea urchin-like tentacles) and hydrogen production performance (58.49 μmol h^{-1} g^{-1}, lower than that of urchin-like $TiO_2/BaTiO_3$ hybrid microspheres, 67.70 μmol h^{-1} g^{-1}), which indirectly demonstrates that the piezoelectric potential due to the local water pressure can enhance the photocatalytic activity.

Above all, the significantly improved hydrogen evolution performance of the $TiO_2/BaTiO_3$ heterostructure is attributed to the coupling effect of two types of piezoelectric potential in the presence of $BaTiO_3$ nanocubes as well as the semiconductor and optical properties of TiO_2 nanowires, which is shown in Fig. 7. It can be inferred that the catalyst can significantly improve the efficiency of converting mechanical energy to chemical energy.

4. Conclusions

Urchin-like $TiO_2/BaTiO_3$ hybrid microspheres were synthesized by assembling nanosized TiO_2 nanowires uniformly and epitaxially onto the surface of tetragonal $BaTiO_3$ nanocubes through a simple hydrothermal method. The piezoelectric potential caused by $BaTiO_3$ nanocrystals in response to ultrasonic waves can act as an alternating internal electric field to incessantly transfer and separate photoinduced carrier pairs (piezoelectric effect). Furthermore, the semiconductor and photonic properties resulting from TiO_2 nanowires (photoelectric conversion) can realize an ultrasonic wave driven piezo-phototronic process and enhance the photocatalytic H_2 generation activity. Moreover, the significant enhancement of photocatalytic hydrogen evolution is due to the coupling effect of two types of piezoelectric potential in the presence of $BaTiO_3$ nanocubes as well as the semiconductor and optical properties of TiO_2 nanowires of the urchin-like $TiO_2/BaTiO_3$ hybrid structure under simulated sunlight and periodic ultrasonic irradiation.

Author contributions

Haidong Li: conceptualization, methodology, writing – original draft, resources, supervision, project administration, funding acquisition. Yanyan Song: investigation, methodology, data curation. Jiyun Zhang: visualization, investigation. Jiating He: writing – reviewing and editing.

Conflicts of interest

The authors declare that they have no known competing financial interests or personal relationships that could have appeared to influence the work reported in this paper.

Acknowledgements

The authors are thankful for funding from the Natural Science Foundation of Shandong Province (Grant No. ZR2018BEM022).

References

1 A. Fujishima and K. Honda, *Nature*, 1972, **238**, 37.
2 Y. Wang, H. Li, G. Chen, Z. Wang, Y. Sang and H. Liu, *Sol. Energy Mater. Sol. Cells*, 2017, **161**, 297–304.
3 H. Li, Y. Wang, G. Chen, Y. Sang, H. Jiang, J. He, X. Li and H. Liu, *Nanoscale*, 2016, **8**, 6101–6109.
4 Y. Zhu, Q. Ling, Y. Liu, H. Wang and Y. Zhu, *Phys. Chem. Chem. Phys.*, 2015, **17**, 933–940.
5 W. Yang, Y. Yu, M. B. Starr, X. Yin, Z. Li, A. Kvit, S. Wang, P. Zhao and X. Wang, *Nano Lett.*, 2015, **15**, 7574–7580.
6 M. Wang, J. Ioccozia, L. Sun, C. Lin and Z. Lin, *Energy Environ. Sci.*, 2014, **7**, 2182–2202.
7 Y. Zhang, M. Wu, Y. Wang, Y. H. Kwok, W. Pan, W. Szeto, H. Huang and D. Y. C. Leung, *Appl. Catal., B*, 2021, **280**, 119388.
8 S. Liang, Y. Shu, K. Li, J. Ji, H. Huang, J. Deng, D. Y. C. Leung, M. Wu and Y. Zhang, *J. Hazard. Mater.*, 2020, **399**, 122967.
9 P. Garcia-Muñoz, F. Fresno, J. Ivanez, D. Robert and N. Keller, *J. Hazard. Mater.*, 2020, **400**, 123099.

10 D. Li, J. Huang, R. Li, P. Chen, D. Chen, M. Cai, H. Liu, Y. Feng, W. Lv and G. Liu, *J. Hazard. Mater.*, 2021, **401**, 123257.
11 J.-h. Li, J. Ren, Y.-j. Hao, E.-p. Zhou, Y. Wang, X.-j. Wang, R. Su, Y. Liu, X.-h. Qi and F.-t. Li, *J. Hazard. Mater.*, 2021, **401**, 123262.
12 X. Zheng, H. Guo, Y. Xu, J. Zhang and L. Wang, *J. Mater. Chem. C*, 2020, **8**, 13836–13842.
13 Z. Zhao, J. Tian, Y. Sang, A. Cabot and H. Liu, *Adv. Mater.*, 2015, **27**, 2557–2582.
14 N. Liu, C. Schneider, D. Freitag, M. Hartmann, U. Venkatesan, J. Muller, E. Spiecker and P. Schmuki, *Nano Lett.*, 2014, **14**, 3309–3313.
15 J. Zhang, Y. Song, X. Dong, H. Jiang, J. Tang and H. Li, *J. Mater. Sci.*, 2020, **55**, 11167–11176.
16 S. Xie, Z. Shen, J. Deng, P. Guo, Q. Zhang, H. Zhang, C. Ma, Z. Jiang, J. Cheng, D. Deng and Y. Wang, *Nat. Commun.*, 2018, **9**, 1181.
17 J. Cheng, Z. Hu, K. Lv, X. Wu, Q. Li, Y. Li, X. Li and J. Sun, *Appl. Catal., B*, 2018, **232**, 330–339.
18 M. Zhu, S. Kim, L. Mao, M. Fujitsuka, J. Zhang, X. Wang and T. Majima, *J. Am. Chem. Soc.*, 2017, **139**, 13234–13242.
19 Y. Li, M. Yang, Y. Xing, X. Liu, Y. Yang, X. Wang and S. Song, *Small*, 2017, **13**(33), 1701552.
20 F. Qin, T. Zhao, R. Jiang, N. Jiang, Q. Ruan, J. Wang, L.-D. Sun, C.-H. Yan and H.-Q. Lin, *Adv. Opt. Mater.*, 2016, **4**, 76–85.
21 Q. Wu, M. S. Siddique and W. Yu, *J. Hazard. Mater.*, 2021, **401**, 123261.
22 G. Yu, F. Hu, W. Cheng, Z. Han, C. Liu and Y. Dai, *Acta Phys.-Chim. Sin.*, 2020, **36**(7), 1911016.
23 Y. Zhao, Y. Zhao, R. Shi, B. Wang, G. I. N. Waterhouse, L.-Z. Wu, C.-H. Tung and T. Zhang, *Adv. Mater.*, 2019, **31**, 1806482.
24 X.-S. Wang, C. Zhou, R. Shi, Q.-Q. Liu and T.-R. Zhang, *Rare Met.*, 2019, **38**, 397–403.
25 H. Li, T. Chen, Y. Wang, J. Tang, Y. Wang, Y. Sang and H. Liu, *Chin. J. Catal.*, 2017, **38**, 1063–1071.
26 Z. Lou, Q. Gu, Y. Liao, S. Yu and C. Xue, *Appl. Catal., B*, 2016, **184**, 258–263.
27 D. Liu, D. Yang, Y. Gao, J. Ma, R. Long, C. Wang and Y. Xiong, *Angew. Chem.*, 2016, **55**, 4577–4581.
28 J. Jiang, X. Tang, S. Zhou, J. Ding, H. Zhou, F. Zhang, D. Zhang and T. Fan, *Green Chem.*, 2016, **18**, 2056–2062.
29 D. C. Lee, I. Robel, J. M. Pietryga and V. I. Klimov, *J. Am. Chem. Soc.*, 2010, **132**, 9960–9962.
30 W. Gao, Q. Liu, S. Zhang, Y. Yang, X. Zhang, H. Zhao, W. Qin, W. Zhou, X. Wang, H. Liu and Y. Sang, *Nano Energy*, 2020, 71.
31 J. Xiong, X. Li, J. Huang, X. Gao, Z. Chen, J. Liu, H. Li, B. Kang, W. Yao and Y. Zhu, *Appl. Catal., B*, 2020, 266.
32 Z. Liang, C.-F. Yan, S. Rtimi and J. Bandara, *Appl. Catal., B*, 2019, **241**, 256–269.
33 S. Li, J. Sun and J. Guan, *Chin. J. Catal.*, 2021, **42**, 511–556.
34 Y. Su, L. Zhang and W. Wang, *Int. J. Hydrogen Energy*, 2016, **41**, 10170–10177.
35 J. Li, L. Cai, J. Shang, Y. Yu and L. Zhang, *Adv. Mater.*, 2016, **28**, 4059–4064.
36 M. Niu, D. Cheng and D. Cao, *Sci. Rep.*, 2014, **4**, 4810.
37 T. Xia, W. Zhang, J. Murowchick, G. Liu and X. Chen, *Nano Lett.*, 2013, **13**, 5289–5296.
38 M. Wang, L. Sun, Z. Lin, J. Cai, K. Xie and C. Lin, *Energy Environ. Sci.*, 2013, **6**, 1211.
39 L. Liu, H. Huang, F. Chen, H. Yu, N. Tian, Y. Zhang and T. Zhang, *Sci. Bull*, 2020, **65**, 934–943.
40 J. Choi, M. Cui, Y. Lee, J. Kim, Y. Yoon, M. Jang and J. Khim, *Ultrason. Sonochem.*, 2018, **43**, 193–200.
41 W. Zhou, Y. Guan, D. Wang, X. Zhang, D. Liu, H. Jiang, J. Wang, X. Liu, H. Liu and S. Chen, *Chem.–Asian J.*, 2014, **9**, 1648–1654.
42 F. He, A. Meng, B. Cheng, W. Ho and J. Yu, *Chin. J. Catal.*, 2020, **41**, 9–20.
43 J. Wang, G. Wang, B. Cheng, J. Yu and J. Fan, *Chin. J. Catal.*, 2021, **42**, 56–68.
44 Z. Wei, J. Liu and W. Shangguan, *Chin. J. Catal.*, 2020, **41**, 1440–1450.
45 L. Liu and X. Chen, *Chem. Rev.*, 2014, **114**, 9890–9918.
46 G. Liu, H. G. Yang, J. Pan, Y. Q. Yang, G. Q. Lu and H. M. Cheng, *Chem. Rev.*, 2014, **114**, 9559–9612.
47 G. Huang, X. Liu, S. Shi, S. Li, Z. Xiao, W. Zhen, S. Liu and P. K. Wong, *Chin. J. Catal.*, 2020, **41**, 50–61.
48 S. He, W. Dong, Y. Guo, L. Guan, H. Xiao and H. Liu, *Nano Energy*, 2019, **59**, 745–753.
49 J. Gao, D. Xue, W. Liu, C. Zhou and X. Ren, *Actuators*, 2017, **6**, 24.
50 W. Wu and Z. L. Wang, *Nat. Rev. Mater.*, 2016, **1**, 16031.
51 L. Wang, S. Liu, Z. Wang, Y. Zhou, Y. Qin and Z. L. Wang, *ACS Nano*, 2016, **10**, 2636–2643.
52 H. Li, Y. Yu, M. B. Starr, Z. Li and X. Wang, *J. Phys. Chem. Lett.*, 2015, **6**, 3410–3416.
53 J. M. Wu, W. E. Chang, Y. T. Chang and C. K. Chang, *Adv. Mater.*, 2016, **28**, 3718–3725.
54 Z. L. Wang, *Adv. Mater.*, 2012, **24**, 4632–4646.
55 P. Wang, X. Li, S. Fan, X. Chen, M. Qin, D. Long, M. O. Tadé and S. Liu, *Appl. Catal., B*, 2020, **279**, 119340.
56 T. S. Rad, Z. Ansarian, R. D. C. Soltani, A. Khataee, Y. Orooji and F. Vafaei, *J. Hazard. Mater.*, 2020, **399**, 123062.
57 G. K. Dinesh, M. Pramod and S. Chakma, *J. Hazard. Mater.*, 2020, **399**, 123035.
58 H. Li, Y. Sang, S. Chang, X. Huang, Y. Zhang, R. Yang, H. Jiang, H. Liu and Z. L. Wang, *Nano Lett.*, 2015, **15**, 2372–2379.
59 H. Liu, C. Hu and Z. L. Wang, *Nano Lett.*, 2006, **6**, 1535–1540.
60 K.-i. Sakayori, Y. Matsui, H. Abe, E. Nakamura, M. Kenmoku, T. Hara, D. Ishikawa, A. Kokubu, K.-i. Hirota and T. Ikeda, *Jpn. J. Appl. Phys.*, 1995, **34**, 5443–5445.
61 K.-S. Hong, H. Xu, H. Konishi and X. Li, *J. Phys. Chem. C*, 2012, **116**, 13045–13051.
62 K.-S. Hong, H. Xu, H. Konishi and X. Li, *J. Phys. Chem. Lett.*, 2010, **1**, 997–1002.